

### 3.1 Introduction

The catalytic properties of AgNPs have been extensively investigated with respect to various reactions [Aditya *et al.* (2015), Christopher *et al.* (2011)]. However, studies on the shape of AgNPs and their catalytic properties have not been emphasized. An attempt has been made recently by Kundu *et al.* (2017) to correlate the shape of Ag nanostructures to their catalytic activity with respect to reduction of nitroaromatics. This is unlike the case of AuNPs, on which there are studies with respect to the effect of variations in size and shape of these nanostructures on their catalytic properties. For example, facet-dependent catalytic activities of AuNPs for the catalytic hydrogenation of 4-nitrothiophenol as a model reaction was investigated [Zhang *et al.* (2014)]. It also emphasizes the role of undercoordinated surface atoms on the catalytic activities of AuNPs. Recent review by Princel *et al.* (2016) summarizes the advances in the area of catalytic properties of anisotropic AuNPs. Control over shape may also lead to better selectivity [Priece *et al.* (2016)].

Furthermore, as elaborated in Chapter-1, the visible range LSPR absorbance of AgNPs is also shape and size dependent. Shape anisotropy may result in the main LSPR peak splitting into more peaks. This is due to the different types of surface conduction electron oscillations sensitive to different orientations of the nanoparticles. For example, nanorods, show oscillations along the major (longitudinal plasmon band) and minor axes (transverse plasmon band) and thereby give rise to longitudinal and transverse plasmonic absorptions [Singh *et al.* (2010)]. This should also affect the plasmonic photocatalytic enhancement/properties of anisotropic AgNPs. As mentioned earlier in Chapter-1, Christopher *et al.* (2011) were the first to demonstrate that Ag nanostructures can use low-intensity visible photons to enhance normal thermally catalyzed commercially important reactions. The possibility of reactions at lower temperatures

meant that the life or stability of catalyst would be increased. Direct plasmonic enhancement of catalytic activity occurs because relaxation of the surface plasmons could result in formation of hot electrons or surface charge carriers in the form of energetic electron hole pair. If the adsorbates are available on the surface of nanoparticles this excitation can be relaxed by transfer of electron density to adsorbates directly [Kreibig and Vollmer (1995)].

This chapter deals with the impact of size and shape of AgNPs on their catalytic and plasmonic photocatalytic properties. Different shapes of AgNPs can be obtained by polyol method in presence of etchants like  $\text{H}_2\text{O}_2$ , chloride ion, bromide ion and  $\text{Cu}^{2+}$  ions [Keunen *et al.* (2014), Tang and Tsuji (2010)]. Therefore, first of all, different amounts of  $\text{Cu}^{2+}$  etchant is used to achieve variation in fraction of different types of anisotropic AgNPs obtained. Anisotropic shapes are also known to form when PVP is used as the stabilizer. Different aspects of catalytic properties of these AgNPs samples are then investigated by using them as catalysts for: (i) *p*-nitrophenol (Nip) reduction by sodium borohydride ( $\text{NaBH}_4$ ), ii) Nip reduction by glycerol (Gly), (iii) Fenton like oxidative degradation of methyl orange (MO). Effect of temperature on the reaction and thereby on activation energies are also discussed. Next, the effect of visible light irradiation on the catalytic activities of these AgNPs is studied. The following discussion outlines, in brief, the importance of these three reactions for testing the catalytic activities of anisotropic AgNPs samples.

Among the available nitroarenes, the reduction of Nip using  $\text{NaBH}_4$  as reductant has been studied extensively as a model pollutant and catalytic reduction reaction. Given its model behavior, this reaction has been used to compare the kinetics of catalytic reduction over various nanoparticles. This study was normally carried out using costly and/or toxic reductants like metal hydrides, metal borohydrides, hydrazine

etc. [Sudhakar *et al.* (2016), Cui *et al.* (2013), Gawande *et al.* (2012)]. Besides its utility as a model reaction, the synthesis of aminoarenes is important because of various important applications such as corrosion inhibition, hair dyeing, and useful intermediates in the pharmaceutical industry etc. [Zaharia *et al.* (2012), Patil *et al.* (2008), Dieckmann *et al.* (1996)]. Therefore, it is desirable that the conventional reaction, in which  $\text{NaBH}_4$  is used as a reductant, be carried out with a green hydrogen source which serves both as reductant and solvent.

Biomass derived chemicals are renewable, environment friendly and probably the most advantageous alternatives for replacing harmful and costly chemicals [Donate (2014), Chen *et al.* (2010b)]. In this respect, glycerol is a promising substance since it is a major byproduct of the biodiesel industries and is also obtained from other industrial processes involving biomass such as during the conversion of cellulose and lignocellulose [Dutta and Pal (2014)]. It exhibits unique combination of desirable properties necessary for use as reducing agent as well as a solvent for synthetic chemistry. Glycerol exhibits high polarity, low toxicity and flammability, high boiling point, ability to form strong hydrogen bonds and to dissolve both organic and inorganic compounds [Díaz *et al.* (2011), Gu and Jérôme (2010), Wolfson *et al.* (2010), Wolfson *et al.* (2009), Wolfson *et al.* (2007a), Wolfson and Dlugy (2007b)]. Thus, glycerol as a hydrogen donor entails easy separation of product, transition metal complex recycling, and microwave assisted reactions. Furthermore, aerobic oxidation of glycerol over catalysts results in a variety of useful products such as dihydroxyacetone, glyceraldehyde, glyceric acid, glycolic acid, hydroxypyruvic acid, oxalic acid, and tartronic acid [Tavor *et al.* (2010), Hekmat *et al.* (2003)]. Current findings in literature suggest that there are only a few reports of nanomaterials used as catalysts in reduction of nitroarenes to aminoarenes using glycerol as the reductant. In most of these studies

glycerol has been used to serve as solvent. A survey of recent literature shows that only a selected group of nanomaterials such as nanoparticles of Ru, Ni, Ir, Fe<sub>3</sub>O<sub>4</sub>-Ni have been used as catalysts for this class of reactions [Sudhakar *et al.* (2016), Pietrowski (2011), Maytum *et al.* (2010), Zweifel *et al.* (2008)].

It has already been mentioned in Chapter-1 that no reports could be found on use of AgNPs catalyzed Fenton like MO oxidative degradation. However, there are publications on H<sub>2</sub>O<sub>2</sub> decomposition over Ag solid catalysts (a Fenton-like reaction) under both alkaline and acidic pH conditions. It is well known that elucidation of such catalytic reactions play an important role in the design of new processes for water treatment. Recently, Yang *et al.* (2013) have also reported the decomposition of H<sub>2</sub>O<sub>2</sub> on Au/carbon catalysts from this perspective. It is believed that these investigations could be a precursor of further studies of Ag nanostructures loaded on different types of supports for treatment of effluent water from dye user industries.

## 3.2 Experimental

### 3.2.1 Synthesis of PVP stabilized anisotropic AgNPs

Material used for the synthesis of AgNPs were Ag(NO<sub>3</sub>) (Merck), (CH<sub>3</sub>COO)<sub>2</sub>Cu.7H<sub>2</sub>O (Merck), ethylene glycol (Merck) and polyvinylpyrrolidone (PVP) (average molecular weight 40,000) (Himedia). All reagents used without further purification and are of analytical reagent grade. To prepare AgNPs sample 49.5 mL of 0.015 M Ag(NO<sub>3</sub>) and 0.5 mL of 0.015 M (CH<sub>3</sub>COO)<sub>2</sub>Cu.7H<sub>2</sub>O and 25 mL 0.48 M PVP (in terms of monomer unit) solutions made in ethylene glycol (EG) and mixed in a 100 mL two necked flask. N<sub>2</sub> gas was bubbled at room temperature for about 30 min to remove oxygen dissolved in the solution. The reaction mixture was then kept in preheated oil bath at 448 K and heated at this temperature with continuous stirring. The oil bath was maintained at 448 ± 3 K for the next 10 minutes. During this process, the

color of the reaction mixture initially turned blue and later to light yellow. Throughout this process, N<sub>2</sub> was continuously bubbled in the reaction mixture flask. The time of heating was such that only the reduction of silver salt could occur. Therefore, the role of the copper salt in this reaction system is that of an etchant. In this preparation protocol for sample C1 the amount of the etchant (CH<sub>3</sub>COO)<sub>2</sub>Cu.7H<sub>2</sub>O was taken such that the initial silver to copper salt solution precursors in ethylene glycol was in the ratio of 99:1 in terms of millimoles (mM). The same procedure was implemented to synthesize AgNP samples C2, C3 and C4. Only the amount of the etchant (CH<sub>3</sub>COO)<sub>2</sub>Cu.7H<sub>2</sub>O was changed such that the initial silver to copper salt solution precursors in ethylene glycol were in the ratio of 90 : 10, 66.5 : 33.5 and 50 : 50 in terms of millimoles for AgNPs sample C2, C3 and C4 respectively. For proper comparison, AgNPs were also prepared in absence of any copper salt as etchant. This AgNPs sample is hereafter denoted by C0.

### **3.2.2 Catalytic reduction and oxidation**

#### **3.2.2.1 Catalytic Nip reduction with NaBH<sub>4</sub>**

For this purpose, 1.85 mL of water was taken in a standard quartz cuvette of 1cm path length. To this 0.1 mL of  $1.2 \times 10^{-3}$  M Nip was added. Then 50  $\mu$ L of NaBH<sub>4</sub> was added. To carry out blank experiment (without catalyst) the UV-visible spectrum of this reaction mixture was monitored at regular intervals for about 70 minutes. Afterward, the actual experiment was carried out in presence of catalyst (50  $\mu$ L of the as prepared C1 AgNPs sol) and the change in absorption spectrum of this reaction mixture was recorded after every 30 sec time interval at 301 K. The same procedure was repeated to monitor the kinetics of the AgNPs catalyzed reaction at four temperatures 297, 301, 305 and 309 K. UV-visible absorption spectra of these solutions were recorded at regular time intervals with the help of Cary 60 UV-vis spectrophotometer

(Agilent Technologies) in the wavelength range of 200–800 nm. Similarly, the complete kinetics for C0 and C2 to C4 AgNPs catalysts was studied.

### 3.2.2.2 Catalytic Nip reduction with glycerol

2 mL of 2.67 M glycerol solution was taken in a standard quartz cuvette of 1 cm path length. To this 0.15 mL of  $1.2 \times 10^{-3}$  M Nip solution was added. Then 0.1 M NaOH solution was added to the above reaction mixture so that the pH of solution turns basic (~8.5). Initially, the UV-visible of the blank experiment, without catalyst, was recorded. Then, the actual experiment in presence of the catalyst was carried out. For this purpose, the cuvette containing the reaction mixture was maintained at 338 K. After this, 50  $\mu$ L of C1-AgNPs (redispersed as 5 mg in 5 mL water) dispersion was added. The absorption spectrum of this reaction mixture was recorded after every five-minute time interval. The same procedure was repeated to monitor the kinetics of the C1-AgNPs catalyzed reaction at four temperatures 323, 328, 333 and 338 K. The catalytic kinetics of C2 to C4-AgNPs (as well as that of sample C0) was also monitored by the same procedure. Experiments were also done at 306 K with all AgNPs catalysts considered in this chapter. This was done to enable comparison with the data generated from the photocatalytic experiments (see section 3.2.3.1).

### 3.2.2.3 Catalytic oxidation of MO dye

Here, 0.14 mmol of MO was taken in a standard quartz cuvette of 1cm path length. This was then diluted by adding 2 mL of water. The pH of this solution was adjusted to ~3 (acidic) by using appropriate volumes of 0.1 N HCl and 0.1 N NaOH. To this 0.1 mL 50 mM H<sub>2</sub>O<sub>2</sub> solution and 50  $\mu$ L of C0-AgNPs catalysts (redispersed as 5 mg in 5 mL water) was then added, the reaction temperature was maintained at 303 K. The absorption spectrum was recorded after every 10 min time interval. The same procedure was repeated to study the catalytic kinetics of C1 to C4 AgNPs. The

activation energy of the reaction is calculated from data obtained by carrying out the above reaction at four different temperatures (303, 308, 313 and 318 K).

### **3.2.3 Visible light enhancement of catalytic reduction and oxidation activities**

Photocatalytic activity was measured by placing the reaction mixture in a four sided quartz cuvette in the photocatalytic chamber such that the reaction mixture was exposed from all the four sides to cool white LED light as per the setup given in Chapter-2. The temperature of the photocatalytic chamber was maintained at 306 K.

#### **3.2.3.1 Photocatalytic enhancement in Nip reduction with glycerol**

The reaction mixture with the catalyst was prepared as given in section 3.2.2.2. The reaction mixture was then irradiated by visible light from cool white LED source (approximately 940 watts/m<sup>2</sup>) in the photocatalytic chamber at 306 K. The absorption spectrum of the reaction mixture was recorded after every 10-minute time interval.

#### **3.2.3.2 Photocatalytic oxidation of methyl orange dye**

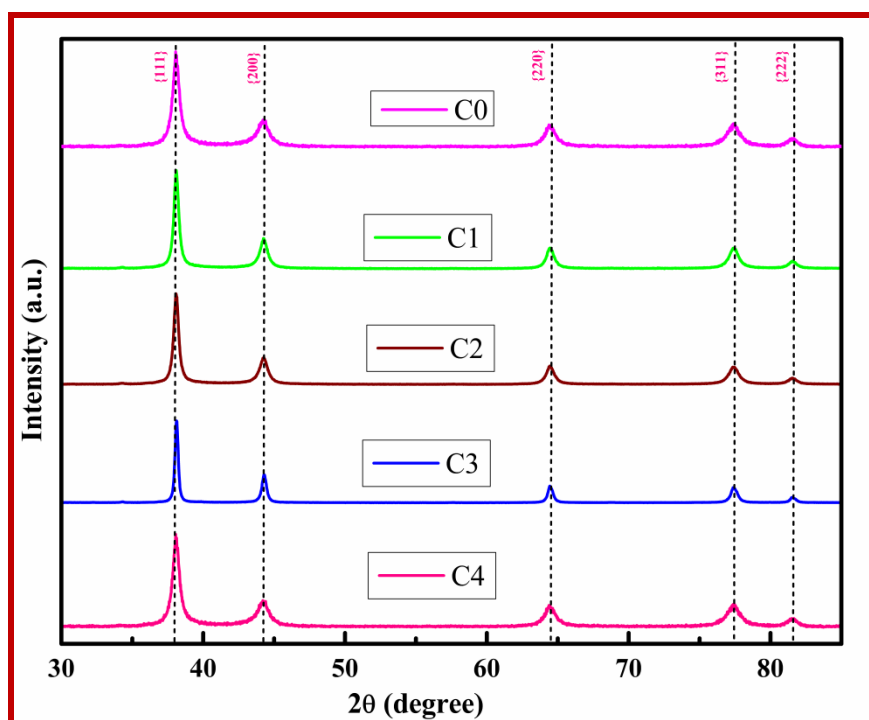
The reaction mixture with the catalyst was prepared as given in section 3.2.2.3. The reaction mixture was kept in the photocatalytic chamber at 306 K and then irradiated by visible light from cool white LED source (approximately 940 watts/m<sup>2</sup>). The absorption spectrum of the reaction mixture was then recorded after every 10-minute time interval. The kinetics and photocatalytic activity were measured for all AgNPs catalysts samples in this manner.

## **3.3. Results and discussions**

### **3.3.1 Characterization of AgNPs**

The X-ray diffraction patterns of the AgNPs powder samples (Figure 3.1) shows peaks at 38.18°, 44.40°, 64.66°, 77.07° and 81.25°. As per XRD data reported for silver

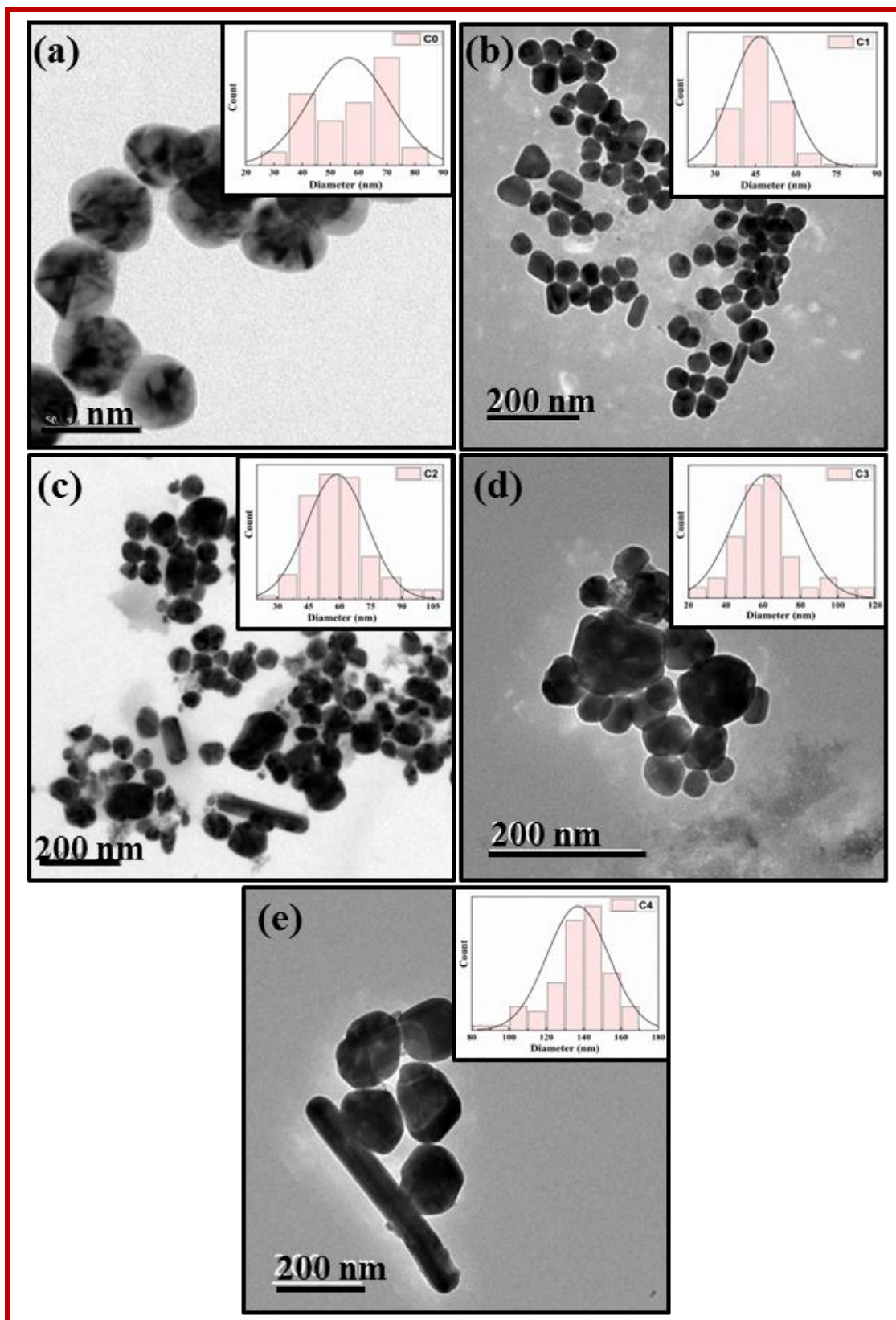
(JCPDS 87-0720), these reflections were correspond to the {111}, {200}, {220}, {311} and {222} planes of FCC silver.



**Figure 3.1** X-ray powder diffraction patterns of C0, C1, C2, C3 and C4 AgNPs

TEM micrographs of C0, C1, C2, C3 and C4 samples are shown in Figure 3.2. The size distribution histograms of the respective AgNPs samples are displayed in inset of these figures. The average size of nanoparticles observed in samples C0, C1, C2, C3 and C4 are ~ 60, ~ 45, ~ 58, ~ 65 and ~ 135 nm respectively. The crystallite sizes of the samples were calculated by the Scherrer's formula. Crystallite sizes for samples C0, C1, C2, C3 and C4 were found to be ~ 16, ~ 14, ~ 15, ~ 17 and ~ 31 nm respectively. Since these sizes are smaller than the average nanoparticle sizes, therefore, it can be concluded that the prepared AgNPs samples are made of multiple crystallites. The AgNPs size increases with the  $\text{Cu}^{2+}$  etchant concentration. Furthermore, the nature of shape anisotropy also changes with the etchant. At low etchant concentration (sample C1) various anisotropic shapes like rod, triangle, square and hexagon are present.





**Figure 3.2** TEM images of C0, C1, C2, C3 and C4 AgNPs shown as 2 (a), 2 (b), 2 (c), 2 (d) and 2 (e) respectively (particle size distributions are shown in inset of their corresponding TEM micrograph).

However, the percentage of spherical faceted particles formed in C1 AgNPs is the largest. Table 3.1 gives the percentage distribution of various anisotropic shapes formed in various AgNPs samples. As the amount of  $\text{Cu}^{2+}$  salt was increased, the percentage of various anisotropic shapes decreased from C1 to C4. In all cases spherical faceted nanoparticles dominate the distribution. In C4, along with some of these shapes, nanowires were also formed.

**Table 3.1.** Percentage of shape distribution present in C0, C1, C2, C3 and C4 AgNPs samples.


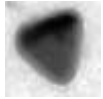
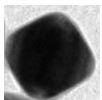
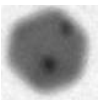
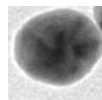

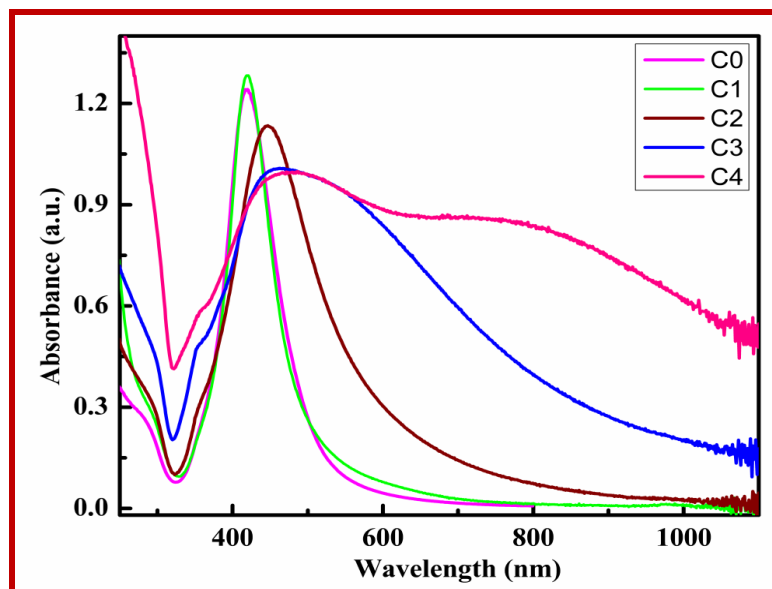
Sr. No.	Catalyst	Rod like 	Triangular 	Cube like 	Hexagon like 	Almost Spherical 	Wire like 
1	C0	--	--	--	--	100	--
2	C1	23	22	4	6	45	--
3	C2	12	15	5	5	63	--
4	C3	13	8	5	10	64	--
5	C4	7	5	3	7	68	10

Figure 3.3 shows LSPR absorbance spectra of aqueous dispersions of AgNPs samples. For samples C0, C1, C2, C3 and C4 LSPR absorbance maxima are observed at  $\sim 418$ ,  $\sim 420$ ,  $\sim 445$ ,  $\sim 465$  and  $\sim 475$  nm respectively. Ag nanostructures display different LSPR bands depending upon the size and shape of nanoparticles. Mock *et al.* (2002) reported that faceted spherical particles show a red shift in LSPR absorbance from  $\sim 410$  to  $\sim 490$  nm with the nanoparticle size variation from  $\sim 40$  to  $\sim 90$  nm.



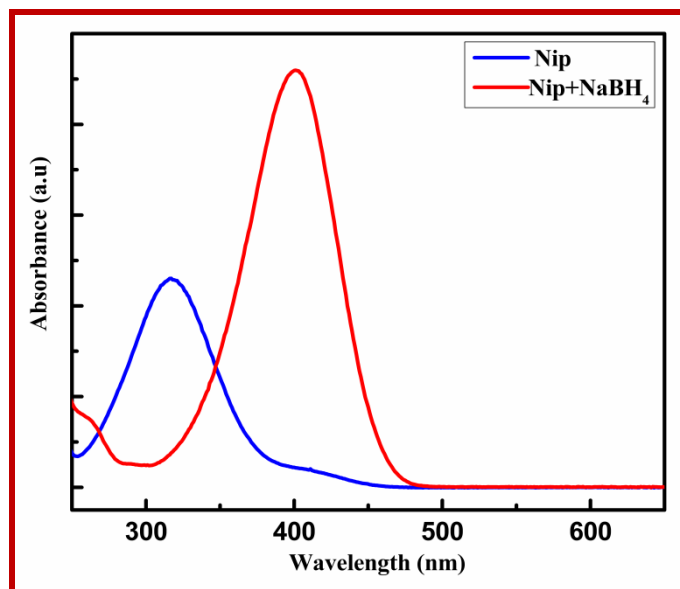
**Figure 3.3** The UV-Vis absorption spectra of aqueous dispersions of C0, C1, C2, C3 and C4 AgNPs sols.

The gradual red shift in transverse LSPR with increase in the average particle size (from C0 to C4) is in agreement with observations in the reference [Mock *et al.* (2002)]. As mentioned earlier, in all the five AgNPs samples nearly spherical shapes are in majority having varied degree of deviation from spherical morphologies. AgNPs sample C1 exhibits maximum number of anisotropic shapes, whereas in other three samples the percentage of anisotropic shapes are less. The LSPR absorbance spectrum of sample C4, owing to the presence of nanowires, displays a longitudinal LSPR at ~ 750 nm [Sun (2010)].

### 3.3.2. Catalytic study

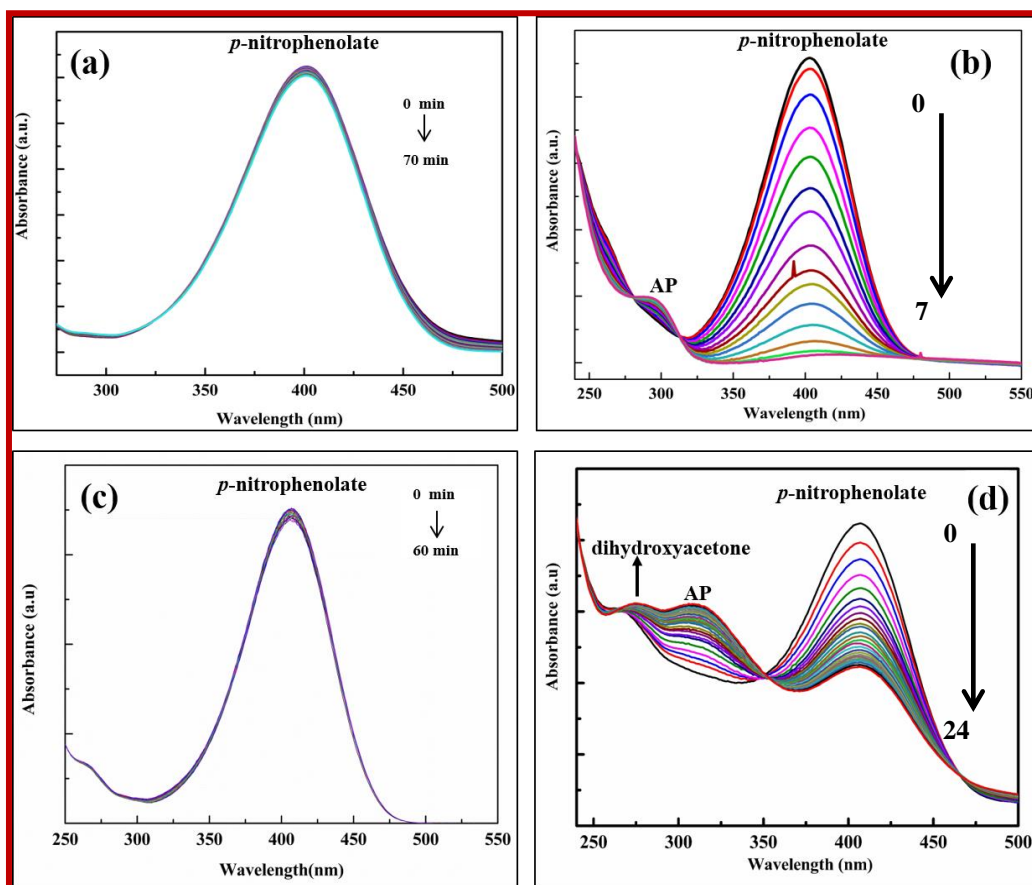
#### 3.3.2.1 Nip reduction with $\text{NaBH}_4$ and glycerol

As prepared Nip solution exhibits a strong absorption peak at ~ 317 nm. Addition of  $\text{NaBH}_4$ , to this Nip solution, results in the shifting of absorbance maximum to ~ 401 nm. This is due to the formation of *p*-nitrophenolate ion (Figure 3.4).



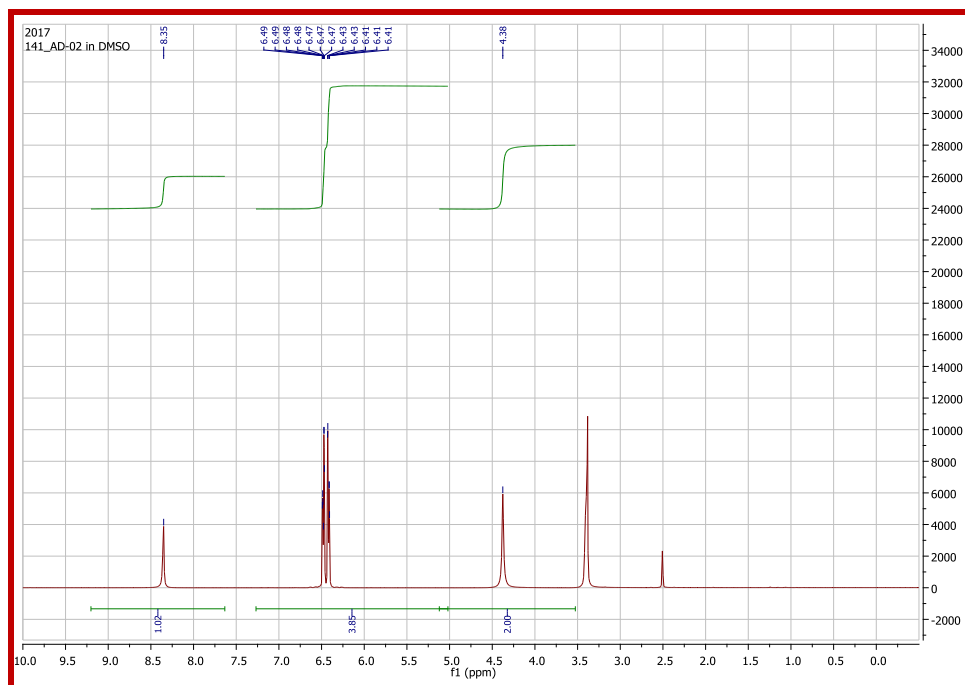
**Figure 3.4** UV absorbance of Nip and *p*-nitrophenolate ion formed after the addition of  $\text{NaBH}_4$ .

The absorbance spectra for Nip reduction with  $\text{NaBH}_4$  and glycerol in absence of catalyst (blank) is shown in Figures 3.5 (a) and 3.5 (c) respectively. The decrease in intensity of absorbance at  $\sim 401$  nm (*p*-nitrophenolate ion) with time, and simultaneously increase in intensity of a new absorbance peak at  $\sim 300$  nm in presence of AgNPs catalyst, showing the formation of AP (Figure 3.5 (b)). This spectrum also displays two isosbestic points at  $\sim 280$  and  $\sim 318$  nm which indicate that Nip was fully converted to AP without any side reaction [Pietrowski (2011)]. Whereas in presence of glycerol as reductant, the decrease in absorbance maximum at  $\sim 406$  nm (*p*-nitrophenolate ion) with time and the formation of absorbance peak at  $\sim 306$  nm with a small hump at  $\sim 274$  nm was observed. The absorbance maximum at  $\sim 306$  and  $\sim 274$  nm shows the formation of AP and dihydroxyacetone respectively (Figure 3.5 (d)). This indicates that Nip was reduced to AP and glycerol was oxidized to dihydroxyacetone in presence of AgNPs as a catalyst (Figure 3.5 (d)).



**Figure 3.5** Variation of absorbance maxima of *p*-phenolate ion (~ 401 nm) with  $\text{NaBH}_4$  reductant in absence (a) and presence (b) of catalyst. Variation in the absorbance maxima of *p*-phenolate ion (~ 406 nm) with Gly as reducing agent in absence (c) and presence (d) of AgNPs catalyst.

However, in this case, the isosbestic points are not clear therefore further characterization was carried out to confirm the formation of AP. First, azo dye test (the qualitative functional group test for aromatic amine group formation) was carried out as per the procedure given in reference [Vogel (1978)] to confirm the reduction of  $-\text{NO}_2$  to  $-\text{NH}_2$ . Formation of orange colored azo dye indicated the presence of aromatic amine functional group. The final confirmation of AP formation was the  $^1\text{H}$ NMR spectrum of the product (Figure 3.6).  $^1\text{H}$ NMR was measured in DMSO,  $\delta$  8.35 (s, 2 H), 7.27 – 5.02 (m, 4 H), 4.38 (s, 2 H).



**Figure 3.6** NMR spectrum of product of Nip reduction with glycerol in presence of C1 AgNPs.

### Reduction kinetics

The general form of rate equation for expressing the kinetics of Nip reduction is given by the following equation.

$$-\frac{\partial A}{\partial t} = k[X]^m[A]^n \quad [3.1]$$

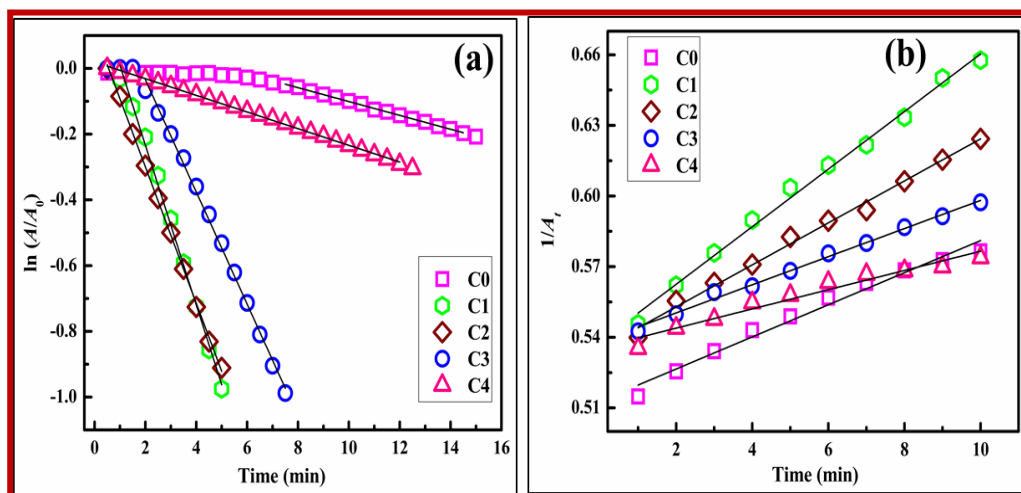
The symbols  $A$  and  $A_0$  denote the absorbance of  $p$ -nitrophenolate ion at time  $t$  and  $t_0$  respectively. The time denoted by  $t_0$  is the induction time ( $t_{ind}$ ) wherever the reduction starts taking place after a time delay. Here,  $X$  denotes the reducing agent ( $\text{NaBH}_4$  or glycerol ( $\text{Gly}$ )),  $k$  is rate constant, the exponents  $m$  and  $n$  give the order with respect to reducing agent [ $\text{NaBH}_4$  or  $\text{Gly}$ ] and reactant [ $\text{Nip}$ ] respectively. As the amount of reducing agent ( $\text{NaBH}_4 \sim 40$  times and 16 wt % glycerol to that of  $\text{Nip}$ ) is in much larger excess than  $\text{Nip}$  concentration taken, therefore the concentrations of reductants remain almost constant during the reaction. Thus, Eqn. 3.1 can be simplified in the following form and integrating the simplified form of Eqn. 3.1 we get Eqn. 3.3.

$$-\frac{\partial A}{\partial t} = k_{app} [A]^n \quad [3.2]$$

$$\ln\left(-\frac{\partial A}{\partial t}\right) = n \ln A + \ln k_{app} \quad [3.3]$$

The slope of the linear fit of  $\ln\left(-\frac{\partial A}{\partial t}\right)$  versus  $\ln(A)$  plot (considering the data points after the elapse of the  $t_{ind}$ ) gives the order  $n$  [Alla *et al.* (2016), Gu *et al.* (2014)] with respect to Nip. The order  $n$  is found to be 1 when  $\text{NaBH}_4$  is the reductant. Accordingly, for  $\text{NaBH}_4$  as reducing agent, the kinetic plots between  $\ln(A/A_0)$  and time are linear for C0, C1, C2, C3 and C4 AgNPs catalyzed reactions (Figure 3.7 (a)). The  $k_{app}$  values were determined from the slopes of the linear fit of  $\ln(A/A_0)$  with time. As mentioned earlier, Nip reduction by  $\text{NaBH}_4$  is a model reaction and majority of catalysts follow pseudo first order kinetics. Therefore, the results obtained for the present catalyst are in agreement with the previous reports in literature [Herves *et al.* (2012), Ghosh *et al.* (2007)]. Furthermore, in all cases where  $\text{NaBH}_4$  was the reducing agent, some induction time was always observed (Figure 3.7 (a)). This is primarily due to adsorption of oxygen in aqueous medium on to the surface of AgNPs [Signori *et al.* (2010)].

On the other hand, the order  $n$  is found to be 2 [using Eqn. 3.3] with Gly as reducing agent. Expectedly, when Gly was the reductant, then the kinetic plots of  $1/A_t$  (Here  $A_t$  is the normalized absorbance  $A$  at time  $t$  with absorbance  $A_0$  at time  $t_0$ ) versus time (for all C0, C1, C2, C3 and C4 AgNPs catalyzed Nip reductions) were found to be linear (Figure 3.7 (b)). In this case, the  $k_{app}$  values were determined from the slopes of the linear fit of  $(1/A_t)$  against time. It is important to point out that no induction time could be observed when Gly was used as the reducing agent. This is because of lower relative solubility of oxygen [Signori *et al.* (2010)] in aqueous solution of glycerol as compared to pure water.



**Figure 3.7** Variation of  $\ln(A/A_0)$  [absorbance ( $A$ ) measured at  $\sim 401$  nm] Vs time with  $\text{NaBH}_4$  reductant **7(a)**. Variation of  $1/A_t$  [absorbance ( $A$ ) measured at  $\sim 406$  nm] Vs time with Gly as reductant in presence of all AgNPs catalyst **7(b)**. The  $R^2$  value of all the fittings is  $\sim 0.98$ .

The  $k_{\text{app}}$  values for reductions carried out using  $\text{NaBH}_4$  and Gly are given in fifth and sixth columns of Table 3.2 respectively. One important aspect must be mentioned before discussing this data. The  $k_{\text{app}}$  values cannot be used to compare the catalytic activity of two different catalysts or the same reaction under different conditions. This is because i)  $k_{\text{app}}$  does not take into account the amount of the catalyst and ii) if the orders of the reactions are different then also comparison is not possible. Hence, the following discussion confines itself to comparison between different AgNPs catalysts studied here for each reducing agent separately.

It can be seen that the  $k_{\text{app}}$  value for C1 AgNPs is the highest in presence of both the reducing agents. The values then decrease from C2 to C3 and further for C4 AgNPs. This correlates well with the increase in nanoparticle size from C1 to C4 (second column in Table 3.2). As the nanoparticle size increases, the surface area of the catalyst and thus the number of surface active sites decreases. The  $k_{\text{app}}$  value of C1 is relatively higher than the rest of the samples. This possibly is because C1 AgNPs has the smallest average nanoparticle size with larger number of anisotropic shapes. As we move from



C1 to C4, the sizes of catalysts increase and the percentage of anisotropic shapes decreases, hence  $k_{app}$  decreases from C1 to C4.

**Table 3. 2.** Average particle size, activation energy and apparent reaction rate constants for Nip reduction with NaBH<sub>4</sub> and Gly as reductant in presence of C0, C1, C2, C3, C4 AgNPs catalyst.

Catalyst	Particle size	Activation energy ( $E_a$ ) (kJ/mol)		Apparent reaction rate constant ( $k_{app}$ )	
	d (nm)	NaBH <sub>4</sub>	Gly	NaBH <sub>4</sub> at 301 K (min <sup>-1</sup> )	Gly at 338K (mol <sup>-1</sup> lit min <sup>-1</sup> )
C0	~ 60	~ 98.9	~ 52.7	0.018	0.0094
C1	~ 45	~ 59.2	~ 25.4	0.243	0.0122
C2	~ 58	~ 71.3	~ 42.3	0.207	0.0089
C3	~ 65	~ 92.2	~ 48.4	0.167	0.0059
C4	~ 135	~ 109.2	~ 61.3	0.0255	0.0041

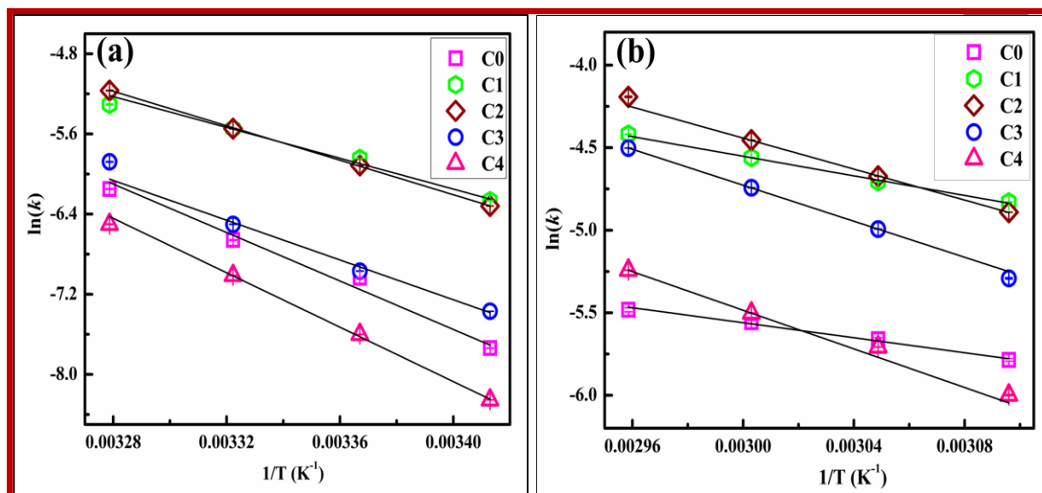
When NaBH<sub>4</sub> was the reducing agent, the lowest  $k_{app}$  value was obtained for C0 AgNPs. However, this was not so when Gly is reducing agent. This indicates that active sites could be different when the reduction is carried out by NaBH<sub>4</sub>, from the case when Gly is the reducing agent. The C0 AgNPs have an average size comparable to C2 and C3 AgNPs. Therefore, it appears that the reduction kinetics by NaBH<sub>4</sub> is affected more by the absence of anisotropic shapes and less by the active sites on faceted spherical nanoparticles. On the other hand, it seems that reduction by Gly is relatively more affected by active sites owing to faceted spherical nanoparticles.

To find the activation energy for Nip reduction, the reactions were carried out at different temperatures with reducing agents (NaBH<sub>4</sub> and Gly) in presence of all AgNPs catalyst. These experiments showed that  $k_{app}$  for all AgNPs catalyst increased with

temperature. The classical Arrhenius equation was employed to find out the activation energies of catalysts. Figure 3.8 (a) and (b) shows  $\ln(k_{app})$  versus  $1/T$  plots for all AgNPs catalyst with  $\text{NaBH}_4$  and Gly reducing agent respectively. A linear plot was obtained in all the cases as per linearized Arrhenius Eqn. 3.4.

$$\ln k_{app} = \ln A - E_a/RT \quad [3.4]$$

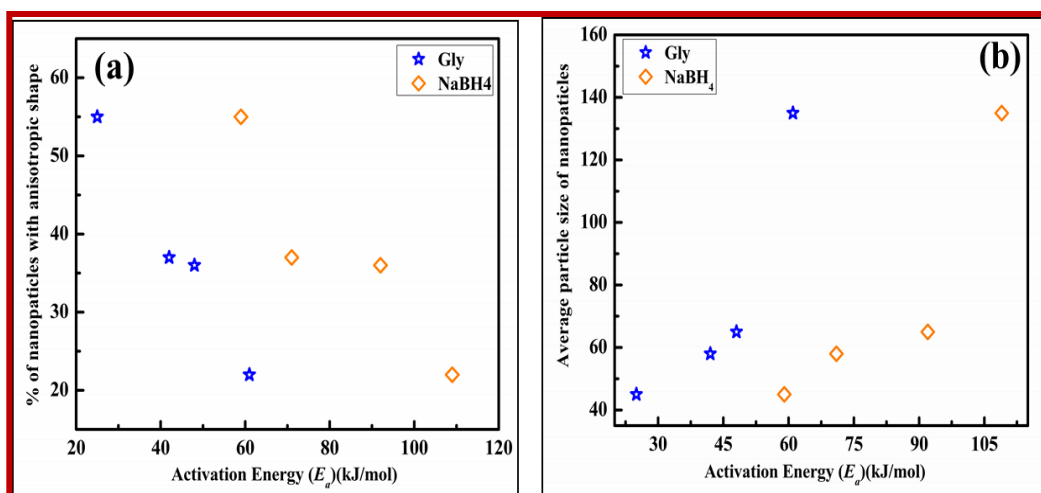
The activation energy ( $E_a$ ) was obtained from the slope ( $-E_a/R$ ) of the linear fits of the  $\ln(k_{app})$  versus  $1/T$  plots. The activation energy increases from C1 to C4 with  $\text{NaBH}_4$  and Gly both. Third and fourth columns of Table 3.2 display the activation energies found when  $\text{NaBH}_4$  and Gly were the reductants respectively. In both the cases, for  $\text{NaBH}_4$  and Gly reducing agent, the  $E_a$  values are lowest for C1 and then increase from C2 to C4. That is,  $E_a$  values increase with decrease in fraction of anisotropically shaped nanostructures in AgNPs sol used as the catalyst. Moreover, for all AgNPs catalyst samples, the  $E_a$  values obtained with  $\text{NaBH}_4$  are greater than those when Gly was the reducing agent.



**Figure 3.8** Arrhenius plot for Nip reduction reaction catalyzed by C0, C1, C2, C3 and C4 AgNPs samples with reducing agents  $\text{NaBH}_4$  (a) and Gly (b). Error bars are very small in most of the cases. The  $R^2$  value of all the fittings is  $\sim 0.98$ .

Sample C1 has the maximum percentage of anisotropic nanoparticles and therefore the least activation energy is observed for this catalyst, whether the reduction was done by  $\text{NaBH}_4$  or by Gly. This is in agreement with previous reports available in literature for catalytic activity of anisotropic nanoparticles. Narayanan and El (2004) also showed that activation energy changes with anisotropic shapes of the catalyst. Furthermore, the activation energy value of C1 is nearly half of the values found for other catalysts in presence of both the reductants. This is possibly due to the larger percentage of smaller anisotropic particles in C1. As mentioned earlier, most studies reported previously in literature are on anisotropic Au nanoparticles.

From the  $E_a$  data in Table 3.2, it appears as if activation energy values of C1 to C4 are correlated with the percentage of anisotropic nanoparticles in AgNPs sample. To verify this, the percentage of nanoparticles with anisotropic shapes (excluding long nanowires) was plotted against activation energy (Figure 3.9 (a)). There seems to be an approximately linear relation between percentage of nanoparticles with anisotropic shapes and their activation energies with both the reducing agents.



**Figure 3.9** Percentage of nanoparticles with anisotropic shapes in all four AgNPs samples (C1 to C4) (a) and average particle size for all four AgNPs samples (C1 to C4) (b) versus their corresponding activation energies ( $E_a$ ).

As mentioned in section 3.1, a comparison of crystallite size from XRD and nanoparticle size from TEM analysis shows that the nanoparticles are composed of multiple crystallites. Therefore, change in  $E_a$  from sample C1 to C4 could also be due to change in grain boundary densities with increase in particles sizes [Feng *et al.* (2016), Feng *et al.* (2015)]. Grain boundaries are high energy regions. The activation energy  $E_a$  could also change due to change in grain boundary density with increase in particle size. To explore whether grain boundaries affect the activation energy or not, the activation energy was plotted against average size of the nanoparticles. The activation energy increases with size of the nanoparticles (Figure 3.9 (b)). This may be because of decrease in grain boundary density with increase in the size of the nanoparticles.

Though in literature, the rate constants ( $k_{app}$ ) are compared for determining the efficiency of different catalysts. It is not a proper measure to define the catalytic activity of the nanomaterials used as catalysts, as the actual amount of catalyst and reactant consumed are not considered in determining the rate constants. The induction time available for some catalyst is also not taken into consideration in finding the rate of the reaction. Therefore, a more appropriate quantity for quantifying the catalytic activity is the turnover frequency (TOF), which includes amount of reactant, catalyst, time required for the conversion of reactant [Eqn. 3.5]. TOF values for all prepared AgNPs catalysts in presence of two reducing agents are given in Table 3.3. These values were calculated by the expression given below:

$$TOF = \frac{\left[ \frac{\text{Number of moles of reactant}}{\text{Number of moles of catalyst}} \right] \times \text{Yield}}{\text{time}} \quad [3.5]$$

The comparisons of reaction conditions and TOF for all the five systems using Gly as the reducing agent are given in Table 3.3. These are also compared with studies reported in literature using Gly for reducing nitroarenes to aminoarenes. Thus, Gawande *et al.*

**Table 3.3** Comparison of turnover frequency (TOF) of different catalyst in transfer hydrogenation reaction of nitroarenes using glycerol as hydrogen source.

Sr. No	Catalyst	Nitroarenes	Reaction Conditions	TOF ( $\times 10^{-2} \text{ min}^{-1}$ )	Reference
1	Fe <sub>3</sub> O <sub>4</sub> -Ni	4-nitrophenol	In glycerol at 353 K	~ 2.4	[Gawande <i>et al.</i> (2012)]
2	Ru/MgLaO	Nitroarenes	In water-10% glycerol at 443 K and inert gas pressure (N <sub>2</sub> gas) 1 MPa in Autoclave.	~ 2.6	[Sudhakar <i>et al.</i> (2016)]
3	Raney Ni	Nitrobenzene	In glycerol at 343 K	~ 0.04	[Wolfson <i>et al.</i> (2009)]
4	C1-AgNPs	4-nitrophenol	In water-16% glycerol at 338 K	~ 0.80	This study
5	C2-AgNPs	4-nitrophenol	In water-16% glycerol at 338 K	~ 0.42	-do-
6	C3-AgNPs	4-nitrophenol	In water-16% glycerol at 338 K	~ 0.27	-do-
7	C4-AgNPs	4-nitrophenol	In water-16% glycerol at 338 K	~ 0.19	-do-

(2016) and Wolfson *et al.* used glycerol as the solvent at temperatures 353 and 343 K respectively. On the hand, Sudhakar *et al.* was used 10 % glycerol as the hydrogen source under inert gas atmosphere and solvothermal conditions at 443 K. In contrast to these available studies in literature, in the present study all reactions were carried out at 338 K with only 16 % glycerol as the reductant. More importantly, the TOF values for all AgNPs catalysts are much higher than the earlier studies. The TOF value of nitroarene reduction using glycerol as hydrogen source was found to be  $2.4 \times 10^{-2}$ ,

$4.37 \times 10^{-4}$  and  $2.6 \times 10^{-2} \text{ min}^{-1}$  in presence of  $\text{Fe}_3\text{O}_4\text{-Ni}$ , Ru/MgLaO and Raney Ni catalyst respectively [Sudhakar *et al.* (2016), Gawande *et al.* (2012), Wolfson *et al.* (2009)]. From Figure 3.9, it was observed that with decreasing percentage of anisotropic shapes the activation energy decreases. Moreover, as one goes from C1 to C4 the AgNPs size also increases, which means that the overall nanoparticle surface area and consequently the number of active catalytic sites also decreases. Owing to a combination of these two factors, the TOF values decrease as we go from C1 to C4.

For the sake of completeness of the study, the TOF values for AgNPs sol catalyzed Nip reduction with  $\text{NaBH}_4$  as the reducing agent, is also given in the Table 3.4. As the catalyst is changed from C1 to C4, the TOF values decrease. Although the values are different, the trend is the same as for Gly given in Table 3.3. As mentioned earlier, from C1 to C4, percentage of anisotropic particles decreases with concurrent particle size increase. Moreover, no comparison is made between values of reactions reduced by Gly and  $\text{NaBH}_4$ . This is because Gly is a green, renewable and much more economical resource, in contrast to the toxic and costly conventional reducing agent  $\text{NaBH}_4$ .

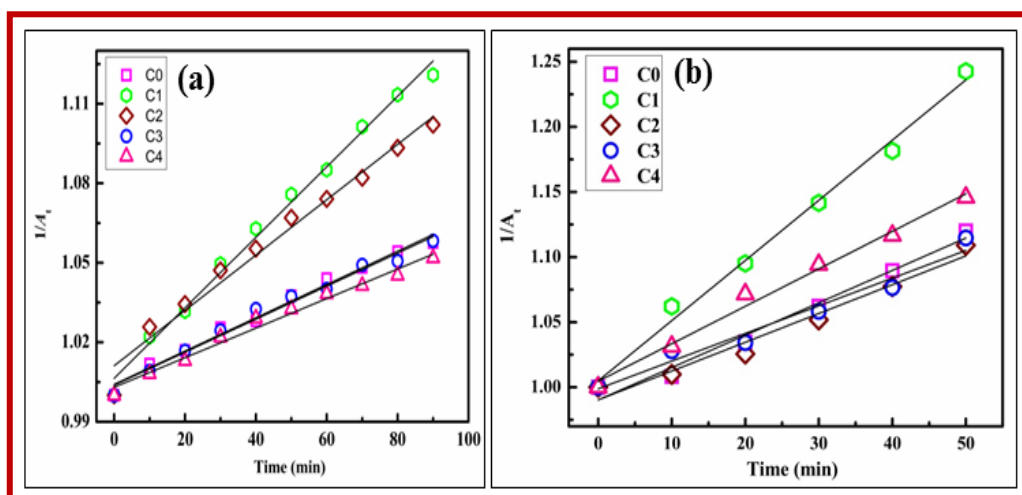
**Table 3.4** Turnover frequency (TOF) of in presence of catalyst and  $\text{NaBH}_4$  as reducing agent at 301 K.

Catalyst	C0	C1	C2	C3	C4
TOF ( $\text{min}^{-1}$ )	~ 160	~ 386	~ 302	~ 258	~ 170

### 3.3.2.2 Photocatalytic study

The first observation to be made is that, as for thermal Nip reduction with Gly, the photocatalytic Nip reduction with glycerol also follows second order kinetics (Figure 3. 10 (b)). This suggests that the basic mechanism of Nip reduction by Gly

remains the same even when it is carried out under visible light irradiation. The second important point that should be noted is that the reactions under visible light were carried out in the photocatalytic chamber at 306 K. The AgNPs catalyzed Gly reduced Nip reactions described in the foregoing sub-section 3.3.2.2 were carried out at temperatures around 338 K. Hence, to investigate the enhancement in catalytic activity owing to visible light irradiation on these AgNPs catalyzed Nip reduction with Gly, this reaction was also done at 306 K (Figure 3. 10 (a)).



**Figure 3.10** Variation of  $1/A_t$  [absorbance ( $A$ ) measured at  $\sim 406$  nm] Vs time in thermal (a) and photocatalytic (b) Nip reduction with Gly. The  $R^2$  value of all the fittings is  $\sim 0.98$ .

The  $k_{app}$  and PTOF (photocatalytic TOF) values of photocatalytic Nip reduction with glycerol are given in columns 3 and 5 of Table 3.5 respectively. For the sake of comparison and determining the enhancement due to visible light exposure, the TOF value for Nip reduction done at 306 K with light exposure is also given in column 4 of Table 3.5. The  $k_{app}$  value for C1 AgNPs is highest due to its smaller size and higher percentage of anisotropic shapes. The TOF value enhancement varies from approximately 80 to 110 %. The PTOF values decrease as the catalyst is changed from C1 to C4. However, the decrease in  $k_{app}$  values from C1 to C3 correlates well with the increase in nanoparticle size from C1 to C3 and decrease in fraction of nanoparticles

with anisotropic shapes. In C4 AgNPs the particle size is bigger but this AgNPs sol sample consists of predominantly nanowires which may be owing to different active sites leading to better plasmonic excitation of electrons. The disparity between PTOF and corresponding  $k_{app}$  values is due to the fact that while former has calculated for 80 % reaction, the latter ( $k_{app}$ ) has been calculated using kinetics data for less than 50 % reaction completion. In general, all AgNPs samples demonstrate significant enhancement in  $k_{app}$  values.

**Table 3.5** Apparent reaction rate constant and turnover frequency (TOF) for thermal and photocatalytic Nip reduction with Gly as reducing agent at 306 K.

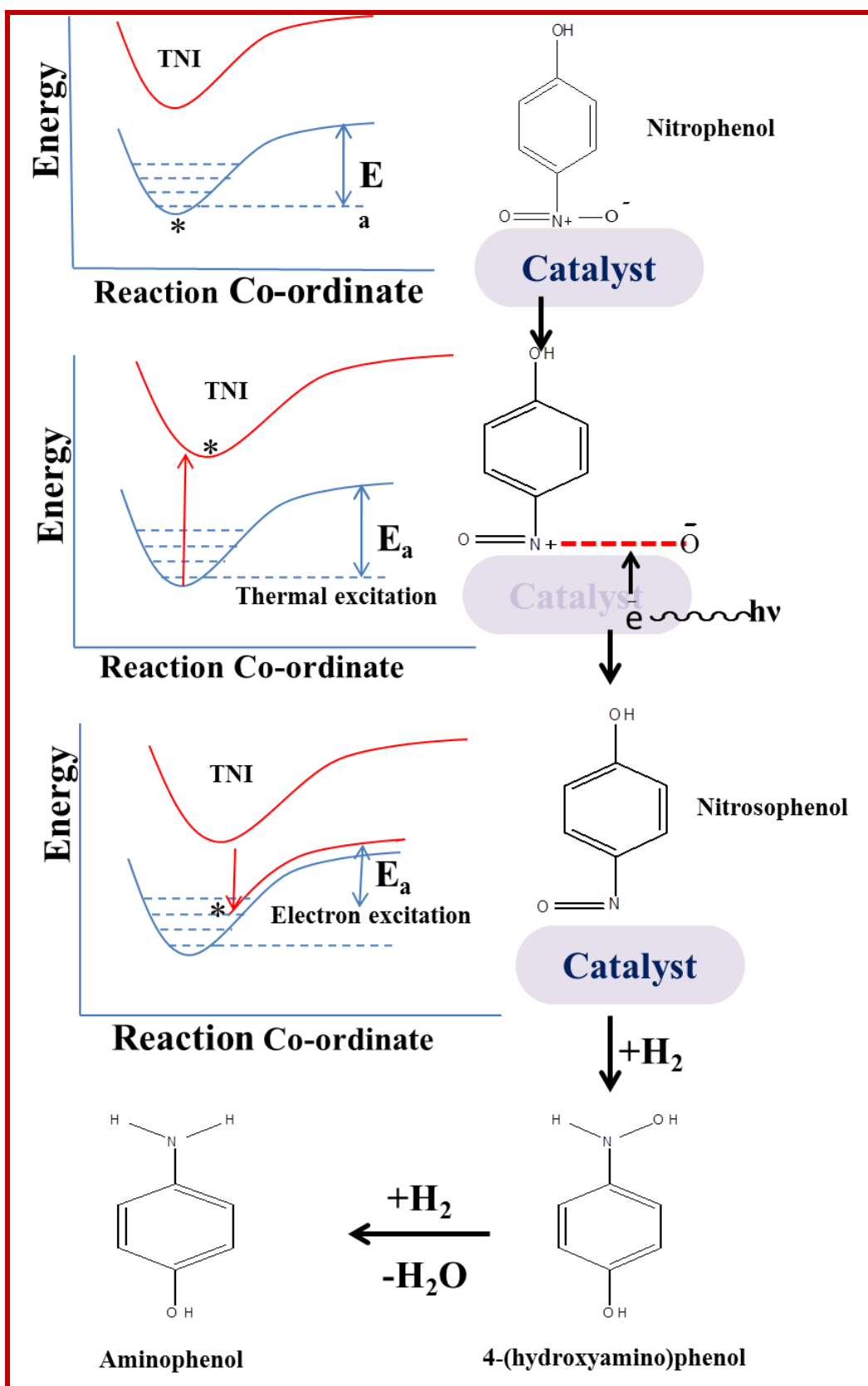
Catalyst	Apparent reaction rate constant ( $k_{app}$ ) ( $\text{mol}^{-1} \text{lit min}^{-1}$ )		Turnover frequency (TOF) ( $\text{min}^{-1}$ )	
	Thermal	Photo	TOF	PTOF
C0	0.00063	0.0024	~ 8.6	~ 15.3
C1	0.00133	0.0046	~ 13.5	~ 21.9
C2	0.00104	0.0022	~ 11.8	~ 20.2
C3	0.00062	0.0021	~ 9.4	~ 19.4
C4	0.00055	0.0028	~ 9.7	~ 17.6

In the present investigation the AgNPs are unsupported, which means that the photocatalytic enhancement occurs due to the presence of plasmonic catalyst. Christopher *et al.* (2011) proposed a mechanism for such photocatalytic enhancement on pure plasmonic materials. These include unsupported plasmonic metals, like the present case, and also those supported on insulators, which allow all the chemistry to happen on the metal nanomaterial. The LSPR absorbance of light by AgNPs can relax either by re-emitting resonant photons (scattering) or forming energetic charge carriers (energetic electrons and holes) at the surface of nanostructures. In the latter case, the



charge carrier can be directly transferred from higher energy levels in the metal to the unoccupied molecular orbital of the adsorbate. The transient negative adsorbate ion thus generated has a short lifetime. The electrons then decay back into the metal Fermi level and the adsorbate returns to the ground state potential energy surface but with increased vibrational energy. Figure 3.11 schematically describes this mechanism. Owing to excited vibrational energy state of the adsorbate the reaction rate is enhanced, even though the reaction occurs at a lower temperature.

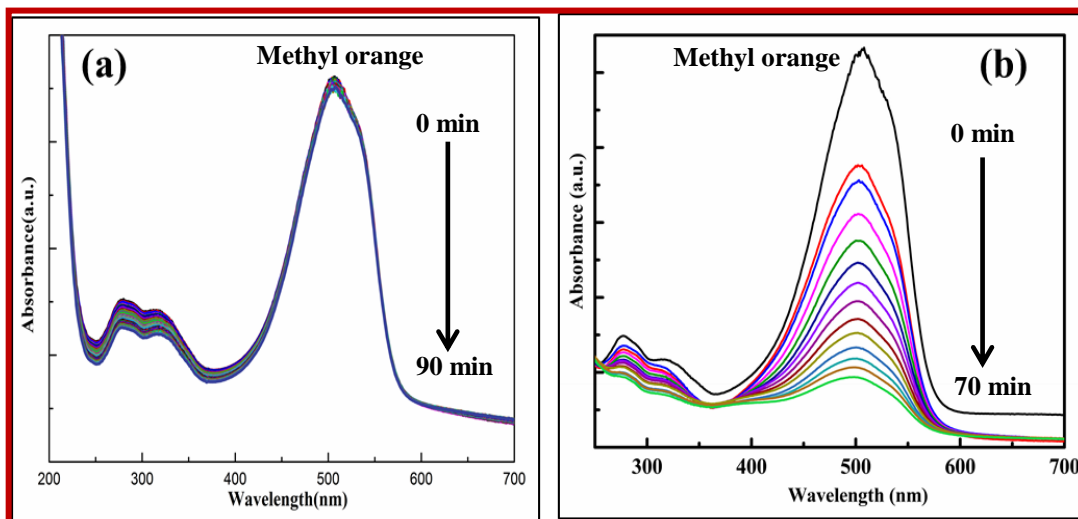
On the other hand, the re-emission of photons can also focus electromagnetic radiation on the adsorbate. Since adsorbed Nip molecules have HOMO-LUMO gap in the visible light, therefore, such re-emission could also excite Nip to facilitate further reaction. The absorption of photons via such allowable electronic transitions can polarize the required bonds in the adsorbates.



**Figure 3.11** Proposed mechanism for electron-induced N-O dissociation on a photo-excited plasmonic metal. 1. Initially ground-state 2. The energetic electron helps in dissociation of N-O bond. 3. Electron decays back to the metal Fermi level.

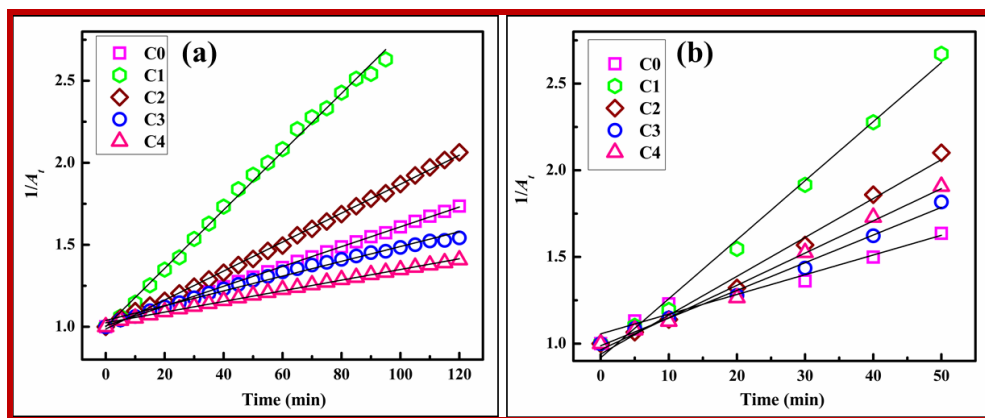
### 3.3.2.3 Metlyl orange oxidation thermal and photocatalytic

Initially a blank experiment was carried out for MO degradation with  $\text{H}_2\text{O}_2$  (in absence of catalyst) only till 90 min (Figure 3.12 (a)). In absence of catalyst MO degradation was found to be negligible. Figure 3.12 (b) shows the UV-visible spectrum of MO degradation when the reaction is carried out in presence of C1 AgNPs.



**Figure 3.12** Variation of absorbance maximum of MO ( $\sim 506$  nm) with  $\text{H}_2\text{O}_2$  oxidizing agent in absence (a) and presence (b) of catalyst C1 AgNPs catalyst.

The peaks initially present in the UV-visible of MO in acidic medium (Figure 3.12 (a)) include the main absorption at  $\sim 506$  nm and also bands at  $\sim 317$  nm and  $\sim 276$  nm in UV region due to  $\pi$  system delocalization. All these peaks in the MO UV-visible undergo degradation together with progress of time in Figure 3.12 (b). Moreover, there is also no sign of any new absorption in these regions.



**Figure 3.13** Variation of  $1/A_t$  [absorbance ( $A$ ) measured at  $\sim 506$  nm] versus time for thermal (a) and photocatalytic (b) MO degradation in presence of C0, C1, C2, C3 and C4 AgNPs catalyst. The  $R^2$  value of all the fittings is  $\sim 0.97$ .

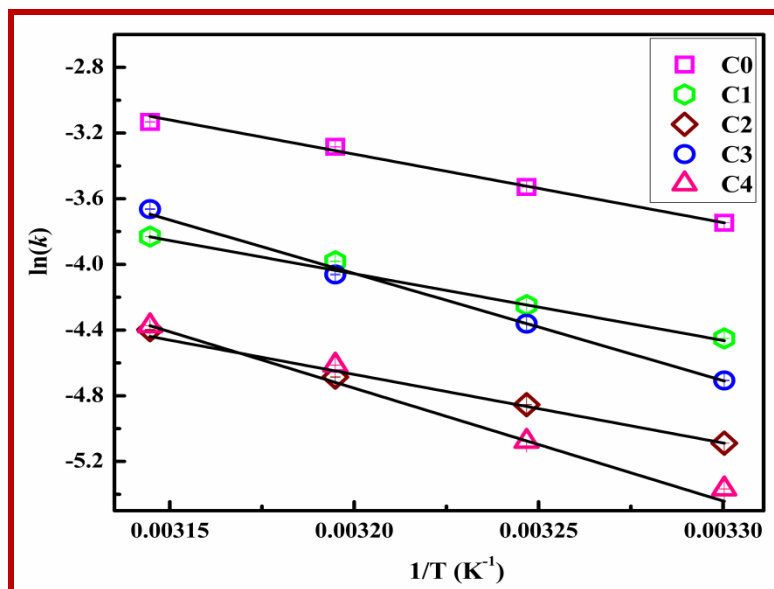
As per Eqn. 3.3, the slope of the linear fit of  $\ln\left(-\frac{\partial A}{\partial t}\right)$  versus  $\ln(A)$  plot gives the order of MO degradation. The order, thus calculated, was found to be 2 for both thermally catalyzed as well as when the reaction was carried out under visible light. Since the order of reaction does not change when the reaction was carried out under visible light, this indicates that the reaction mechanism is unaltered. Being second order,  $1/A_t$  versus time for all C0, C1, C2, C3 and C4 AgNPs catalyzed thermal and photocatalytic MO degradations were plotted. The plots were found to obey good linear fits (Figure 3.13) and the  $k_{app}$  values were obtained from the slopes of these linear fits. The  $k_{app}$  values of both thermal and photocatalytic MO degradation are tabulated in Table 3.6. Last two columns of Table 3.6 display the TOF and PTOF values obtained. The  $k_{app}$  value for C1 AgNPs is again the highest in both, thermal and photocatalytic oxidative degradation of MO. The  $k_{app}$  value in thermal catalytic degradation of MO in presence of C2 AgNPs is half of C1 and for C3 it is almost half of C2 and further decreases from C3 to C4. This again correlates with size which increases from C1-C4 and decrease in number of anisotropic shapes from C1-C4 AgNPs sample.

**Table 3.6** Apparent reaction rate constant, activation energy and turnover frequency (TOF) for thermal and photocatalytic MO degradation at 306 K in presence of all AgNPs catalyst.

Catalyst	Apparent reaction rate (mol lit <sup>-1</sup> min <sup>-1</sup> ) ( $k_{app}$ )		Activation energy ( $E_a$ ) (kJ/mol)	Turn over frequency (min <sup>-1</sup> )	
	Thermal	Photo		TOF	PTOF
<b>C0</b>	0.0060	0.0111	~ 34.7	~ 1.5	~ 3.0
<b>C1</b>	0.017	0.0326	~ 33.7	~ 3.0	~ 6.0
<b>C2</b>	0.008	0.0213	~ 34.6	~ 1.8	~ 5.8
<b>C3</b>	0.0045	0.0151	~ 54.2	~ 1.2	~ 2.8
<b>C4</b>	0.0033	0.0182	~ 57.1	~ 1.0	~ 3.2

Whereas in photocatalytic degradation this decrease is from C1 to C3 and then it increases for C4. Similar trends are observed for TOF and PTOF values as well. The important thing is the enhancement obtained when catalytic oxidative MO degradation was carried out under visible light. The enhanced PTOF values are almost 2 to 3 times of thermal TOF values.

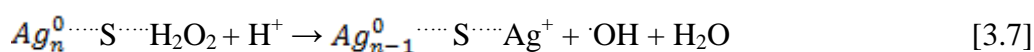
Activation energies are calculated utilizing Arrhenius equation. The plot between  $\ln(k_{app})$  versus  $1/T$  is shown in Figure 3.14. The  $E_a$  values increase from C1 to C4, in accordance with decrease in fraction anisotropic nanoparticles in the AgNPs and also their concurrent increase in average particle sizes.

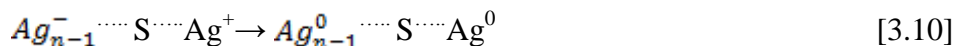
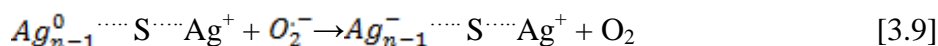
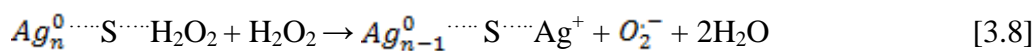


**Figure 3.14** Arrhenius plot for MO degradation catalyzed by C0, C1, C2, C3 and C4 AgNPs samples. Error bars are very small in most cases. The  $R^2$  value of all the fittings is  $\sim 0.98$ .

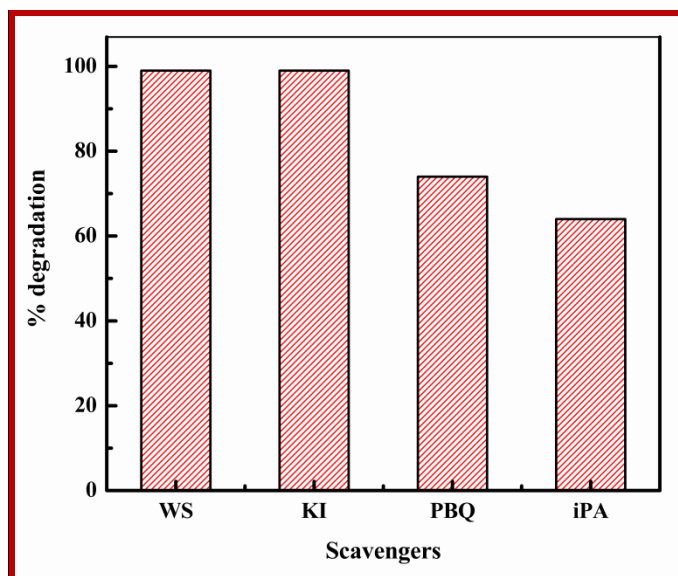
### 3.4 Mechanism involved

As mentioned earlier, no reports in literature could be found on oxidative catalytic degradation of MO. However, He *et al.* (2014a) reported Fenton like, generation of hydroxyl radical through zero-valent AgNPs under acidic condition. These authors commented that most likely the interaction of the stabilized AgNPs with  $H_2O_2$  leads to oxidation of some Ag atoms on the surface of the nanoparticles. Consequently, the formed  $Ag^+$  is located at the surface of the AgNPs. The possible reaction mechanism involved in catalytic degradation of MO in the present study, based on this, is given below. ‘S’ represents the stabilizer molecule attached to the AgNPs in equations given below:





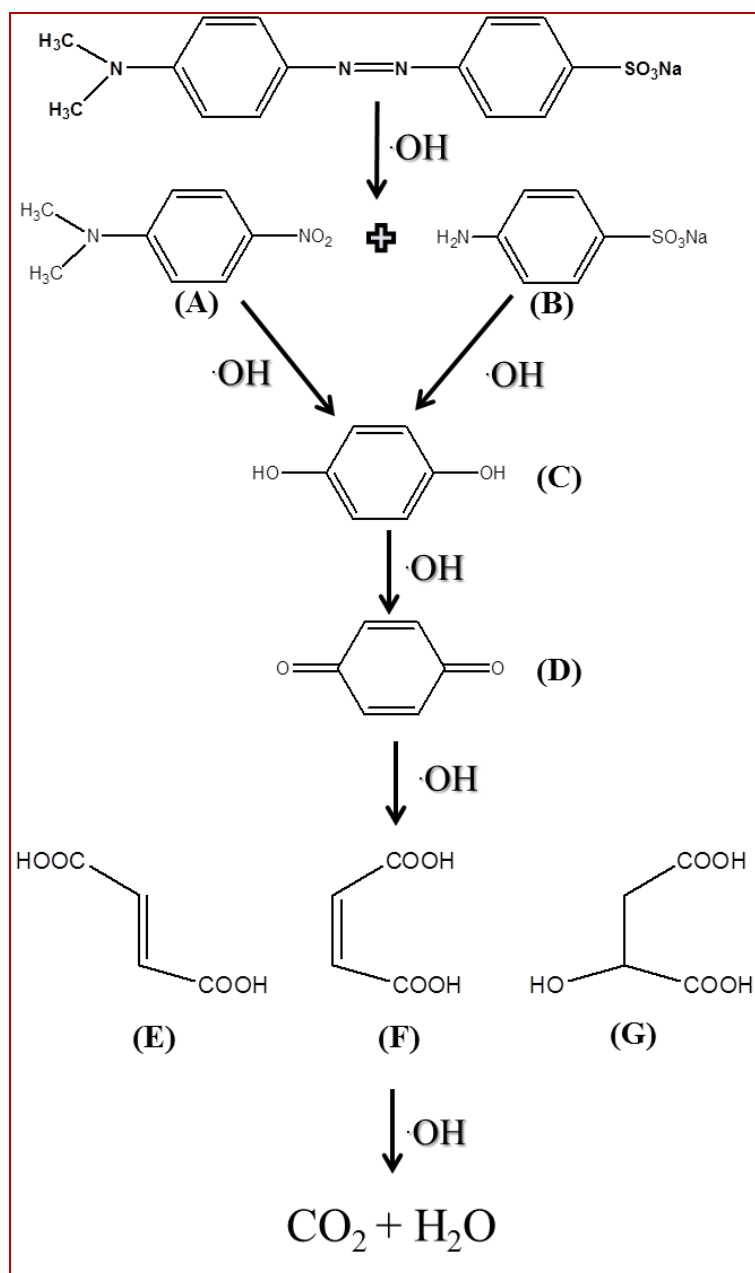
From the above it is inferred that the hydroxyl radicals generated are responsible for MO degradation. To confirm this, active species generated during MO degradation were investigated. For this purpose *p*-benzoquinone (PBQ), potassium iodide (KI) and isopropyl alcohol (iPA) were used as scavengers to capture superoxide radical ( $O_2^-$ ), holes, and hydroxyl radicals ( $\cdot OH$ ) respectively. Degradation efficiency was most affected by addition of iPA, which shows that the main active species for this reaction is  $\cdot OH$  (Figure 3.15).



**Figure 3.15** Percentage photocatalytic MO degradation without scavenger (WS) and in presence of KI, PBQ and iPA scavengers

For such hydroxyl radical based MO degradation, Wang *et al.* (2014) have suggested the following mechanism. The schematic of this mechanism is shown in Figure 3.16. It is important to mention here that if the degradation had stopped at either stage (A, B) or C or D, then the MO degradation UV-visible spectra would have shown

the emergence of a new peak. However, as mentioned earlier, no such peak could be observed in Figure 3.12 (b). This indicates that the MO must have been degraded at least till stage (E, F, G).



**Figure 3.16** Proposed mechanism for the oxidative degradation of MO with  $\text{H}_2\text{O}_2$  in presence of AgNPs catalyst. Complete degradation of MO gives carbon dioxide and water through intermediates: (A) N,N-dimethyl-4-nitrobenzeneamine, (B) Sodium 4-aminobenzenesulfonate, (C) Hydroquinone, (D) Cyclohexa-2,5-diene-1,4-dione, (E) Fumaric acid, (F) Maleic acid and (G) 2-hydroxysuccinic acid



### 3.5 Mechanism for Photocatalytic enhancement

As mentioned earlier, the order of the reaction does not change when the catalytic oxidation is done under visible light or without light. Additionally, the active species determination experiments also show that hydroxyl radicals are responsible for MO degradation both in visible light as well as without light. In view of this, it may be said that the basic mechanism remains the same in both cases. In view of this, the following mechanism is perhaps occurring. That is, visible light LSPR absorbance by AgNPs leads to formation of energetic charge carriers. Some of these electrons are then directly transferred from higher energy levels in the metal to the unoccupied molecular orbital of the adsorbate resulting in formation of hydroxyl radicals. In this case, the visible light plasmonic excitation possibly facilitates step (2) of the reaction mechanism given in sub-section 3.3.2.3. This involves, the oxidation of some Ag atoms on the surface of the AgNPs and thereby generation of hydroxyl radicals in acidic pH. The oxidized surface Ag atoms are reduced back in step (5) resulting in regeneration of AgNPs.

### 3.6 Conclusions

Anisotropic AgNPs have been found to act as efficient catalysts for Nip reduction and MO oxidation. The AgNPs were synthesized by a polyol process in presence of different amounts of  $\text{Cu}^{2+}$  salt etchant. The percentage of particles with anisotropic shapes decreases with the amount of etchant. The average nanoparticle size increased with etchant concentration and on excess etchant use nanowires were also formed. All AgNPs samples were found to catalyze Nip reduction and MO oxidation. The rate of the reaction decreases with increase in average size of the nanoparticles due to consequent decrease in surface active sites. At the same time, with decrease in

percentage of particles having anisotropic shapes in the catalyst sample there is concomitant increase in activation energy of the reaction. An approximately linear relation has been found between the percentage of nanoparticles with anisotropic shapes and activation energy. Overall the efficacy of the catalyst decreased with increase in average particle size and decrease in extent of anisotropy. In contrast to the conventional reaction with  $\text{NaBH}_4$  as the reducing agent, this reaction with glycerol hydrogen source follows second order kinetics with respect to  $\text{Ni}^{2+}$ . Due to plasmonic effect of AgNPs photocatalytic enhancement is also observed in presence of both reductants. MO oxidation also follows second order kinetics in thermal as well as photocatalytic reaction. Photocatalytic MO degradation also shows enhancement in PTOF compared to thermal TOF.